ACS MATERIALS LETTERS

www.acsmaterialsletters.org

In Situ Generation of Flash Graphene Supported Spherical Bismuth Nanoparticles in Less than 200 ms for Highly Selective Carbon Dioxide Electroreduction

Miao Wang,[#] Huaizhu Wang,[#] Yating Gu,[#] Mengfei Zhu, Mohan Kumar, Junchuan Liang, Zuoxiu Tie, Jing Ma,* and Zhong Jin*

Cite This: *ACS Materials Lett.* 2024, 6, 100−108

Read Online

ACCESS | Metrics & More | Article Recommendations | Supporting Information

ABSTRACT: **Flash Joule heating (FJH) method is an emerging and powerful technique that has exhibited great potential in various domains. Herein, we successfully prepared flash graphene (FG)-supported Bi nanoparticles (Bi-NPs/FG) via the ultrafast and ecofriendly FJH method in less than 200 ms for the first time. Benefited from the synergistic effect of highly conductive FG and active Bi nanocrystals, the Bi-NPs/FG hybrid shows a highly selective CO_2 electroreduction with an ultrahigh Faradaic efficiency of 93.8% toward C1 product (i.e., formate). Furthermore, the findings from Density Functional Theory (DFT) calculations unveil that the reconstruction process not only enhances the bonding strength of the surface Bi-OCHO*, but also optimizes the adsorption energy of the key intermediate (OCHO*), thus benefiting the production of formate. In addition, we conducted an extension study of the FJH route to demonstrate its versatility in preparing a range of other metal/alloy NPs encased in FG. This work presents a feasible pathway to the superfast and massive production of highly efficient electrocatalyst for CO_2 conversion, and it can be extended to other application scenarios with great potential.**

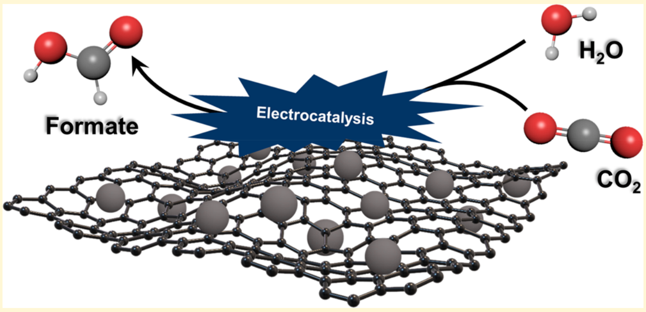

Today, chemical manufacturing often involves an energy-intensive process that requires high pressure and temperature, resulting in the large-scale emission of greenhouse gases (i.e., CO_2) into the atmosphere.[1−3] Thus, the development of innovative technologies toward CO_2 valorization is critical for achieving a carbon-neutral energy cycle and reducing the overdependence on finite fossil fuels during chemical production. It was predicted that by midcentury, two-thirds (67%) of electrical energy would come from renewable energy sources, such as solar photovoltaic, wind, and hydro, according to the International Energy Agency report.[4,5] Therefore, the use of electricity-driven CO_2 transformation and upgrading, i.e., the electrocatalytic CO_2 reduction reaction (CO_2RR), for the production of value-added chemicals is a promising alternative pathway to mitigate the ever-increasing energy crisis and expedite the achievement of carbon neutrality. However, the practical deployment of the CO_2RR is hindered by the high activation energy required for the activation of thermodynamically stable CO_2 molecules and the competing hydrogen evolution reaction (HER) in an aqueous solution.[6,7] Given that, it is crucial to rationally design and develop efficient electrocatalysts with formate being a major product that is considered a perfect hydrogen storage molecule due to its high energy density and easy accessibility.[8,9] Bi-based electrocatalysts hold great potential for the CO_2RR because of their preferred *OCHO formation and weak *HCOOH binding capability but with the limitation of unsatisfactory Faradaic efficiency and stability.[10−12]

We propose a solution to this bottleneck by merging Bi nanostructures with graphene to fabricate a matrix and metal interface composite, thereby benefiting the further enhancement of electrocatalytic performance toward the CO_2RR. As an emerging technique of electrothermal synthesis, the flash Joule heating (FJH) method was first reported by Tour group in

Received: October 3, 2023
Revised: December 2, 2023
Accepted: December 4, 2023
Published: December 6, 2023

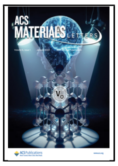

https://doi.org/10.1021/acsmaterialslett.3c01183
ACS Materials Lett. 2024, 6, 100−108

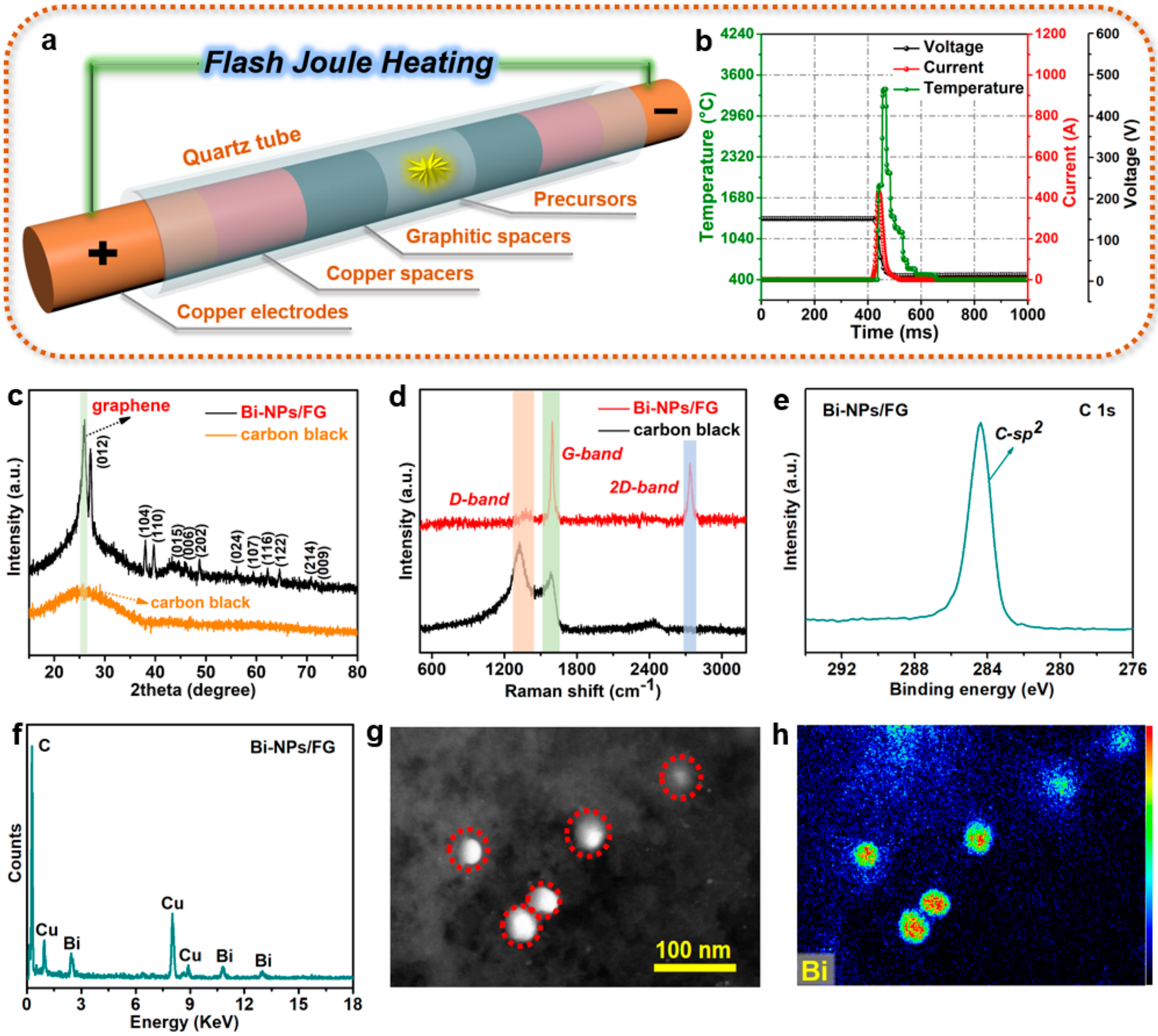

Figure 1. (a) Schematic illustration of a typical FJH reaction device. (b) Real-time temperature, voltage, and current profiles during the direct FJH synthesis of Bi-NPs/FG composite. (c) XRD patterns and (d) Raman spectra of Bi-NPs/FG composite and commercial CB, respectively. (e) High-resolution C 1s spectrum (XPS) of Bi-NPs/FG composite. (f) EDX spectra for Bi-NPs/FG composite with the signal of Cu derived from the TEM grid. (g) Characteristic SEM and (h) corresponding elemental mapping result of Bi-NPs/FG composite.

2020, and it has since found many application scenarios to date, including massive production of flash graphene (FG),[13,14] transforming polymers into graphitic 1D materials,[15] urban mining from the wastes,[16,17] high-performance supercapacitors,[18] and electrochemical oxygen reduction reaction (ORR).[19] Beyond the conventional synthetic methods for electrode materials, the FJH technique presents several significant advantages, such as a rapid reaction process, ease of operation, and batch production of high-quality FG in high yield.

Herein, we report the successful instantaneous preparation of Bi metal nanoparticles (Bi-NPs) wrapped in FG, by utilizing the FJH method in less than 200 ms. The FG obtained here possesses a rotational mismatch feature between neighboring graphene sheets that can efficiently prevent the self-aggregation and surface oxidation of Bi-NPs, thus leading to high structural stability and fast charge transfer kinetics during electrocatalysis processes. The resulting Bi-NPs/FG composite exhibits superior Faradaic efficiency for formate production ($FE_{Formate}$) of 93.8% at a moderate potential of −1.3 V (vs. reversible hydrogen electrode, RHE) in an aqueous solution with a current density of 12.6 mA cm^{-2}, and good long-term stability stemmed from the synergy effect. To gain further insight into intrinsic electrochemical mechanisms of electrode materials, DFT calculations were conducted to explore the origin of enhanced CO_2RR performance for the Bi-NPs/FG catalyst. On the other hand, we extended this ultrafast and ecofriendly FJH method to synthesize various other FG-wrapped precious or nonprecious metal/alloy NPs including Cu, Pt, MnFeCoNiCuZn, and PtPdRhRuAu, suggesting the general applicability of this method in the synthesis of electrode materials for energy conversion and catalysis.

Figure 1a displays a schematic diagram of a typical FJH reactor, comprised of copper spacers, graphitic spacers, a quartz tube, and copper electrodes, while a digital photograph of the FJH system is shown in Figure S1. To prepare precursor materials, carbon black (CB) and bismuth nitrate pentahydrate ($Bi(NO_3)_3 \cdot 5H_2O$) were utilized as carbon and metallic sources, respectively. Figure 1b presents the real-time temperature, current, and voltage data recorded during the experi-

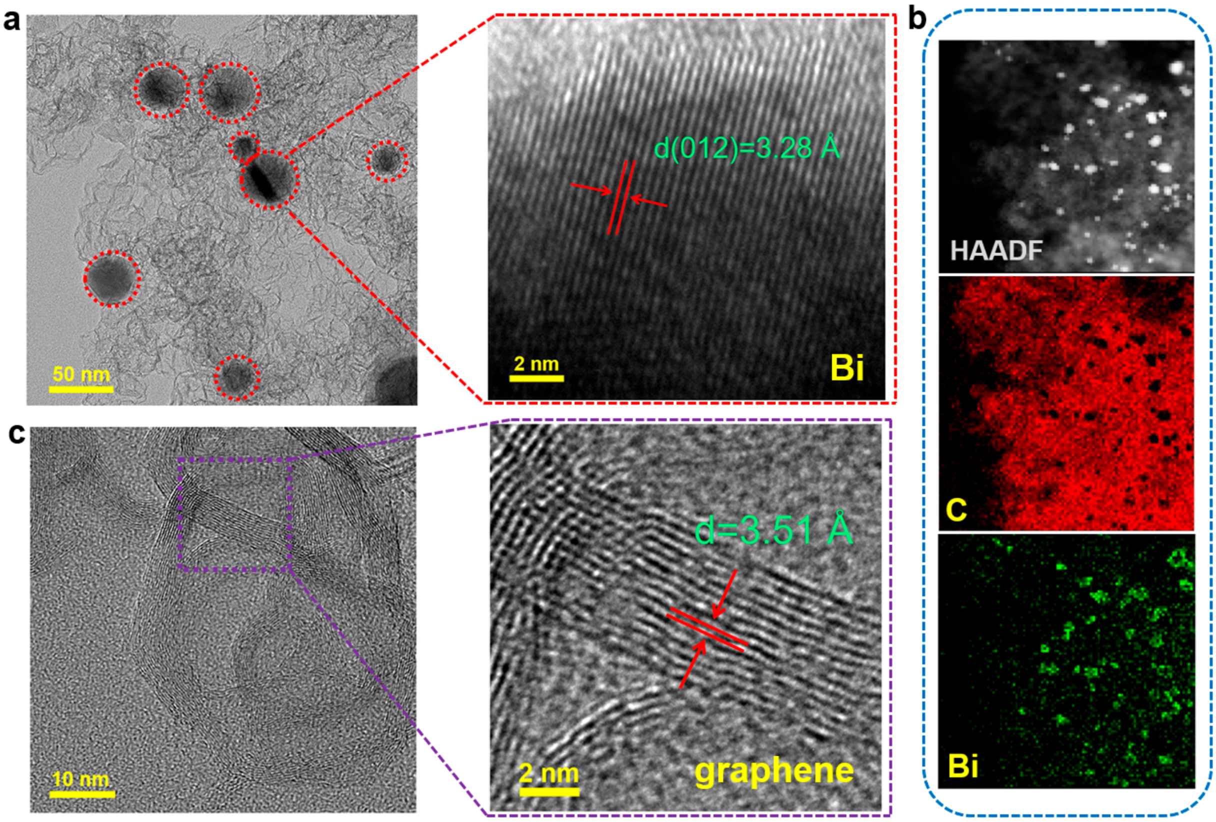

Figure 2. (a) Characteristic TEM and HRTEM images of the Bi-NPs/FG composite. (b) HAADF-STEM image and corresponding elemental mapping results of the Bi-NPs/FG composite. (c) Characteristic TEM and HRTEM images displaying the morphology of FG in the Bi-NPs/FG composite.

ment. During the reactions, the electrodes were linked to a capacitor bank and charged to 150 V. The discharge operation of the capacitor bank initiated an ultrafast heating process (above 3300 °C) of the precursors in less than 200 ms. X-ray diffraction (XRD) technique was utilized to examine the crystalline structure and phase composition of the Bi-NPs/FG composite. The XRD analysis did not reveal any clear signals for the impurity phases. In particular, the observation of a sharp (002) peak along with a weakening (100) peak at around 43° indicate characteristic signals of graphene and confirm the absence of ordered AB-stacking of basal planes, as shown in Figure 1c.[20,21] Meanwhile, the commercial CB phase exhibited only broadening of the (002) peak in comparison with the FG phase. Furthermore, the XRD pattern for Bi moiety in Figure 1c is well-consistent with a rhombohedral Bi crystal structure (JCPDS card no. 44−1246, $R\bar{3}m$, $a = b = 4.5$ Å, $c = 11.8$ Å, $\beta = 120°$), and indicates the nonexistence of oxidized Bi components.

Figure 1d displays the Raman spectrum of CB, revealing the detected signals of high-intensity D band (~1324 cm^{-1}) and G band (~1589 cm^{-1}).[19] The as-synthesized Bi-NPs/FG sample retains the sharp G peak and shows a characteristic 2D peak (~2738 cm^{-1}) corresponding to the second-order zone boundary phonons of graphene, while the D peak is strongly suppressed. The intensity ratio of I_{2D} and I_G is close to 1.0, indicating a good quality and few layered characteristics of graphene sheets, respectively.[22] The I_D/I_G value of CB was calculated to be ~1.3, which is obviously greater than that of FG obtained here, illustrating the elimination of various structural disorders or defects via the FJH method. Furthermore, X-ray photoelectron spectroscopy (XPS) was employed to investigate the phase characteristics of Bi-NPs/FG. The observed main peaks of Bi 4f$_{7/2}$ and Bi 4f$_{5/2}$ located at ~158.6 eV and ~164.0 eV (Figure S3), respectively, further verifying the zerovalent state of metallic Bi.[11,23] High resolution C 1s spectra display a symmetric feature (Figure 1e), where the detected main peak at 284.4 eV corresponds to the typical sp^2-bonded carbon, demonstrating the successful transformation from amorphous carbon to graphene.[18,24,25] The energy-dispersive X-ray (EDX) spectra confirm the presence of C and Bi elements in the composite, while the Cu signal is attributed to the TEM grid (Figure 1f). The microstructure of Bi-NPs/FG composite shown in Figure 1(g−h) reveals the Bi-NPs wrapped in FG, which are well-dispersed in the graphene framework without self-agglomeration and are estimated to have a diameter range of 20−50 nm. The particle size distribution of the as-obtained Bi-NPs/FG sample is displayed in Figure S4.

Transmission electron microscopy (TEM) image in Figure 2a of the as-synthesized hybrid illustrates that the dark spherical Bi-NPs, highlighted by dotted circles, are enveloped by FG, which aligns well with the SEM image referred to above. This observation further confirms the uniform dispersion of Bi nanocrystals in the graphene matrix. The corresponding high-resolution TEM (HRTEM) image of the Bi-NPs/FG composite shows a clear crystal lattice with *d*-spacing of 3.28 Å, which is assigned to the (012) planes of Bi crystal. The high angle annular dark field-scanning transmission electron microscopy (HAADF-STEM) combined with EDX mapping images of the FG supported Bi-NPs are shown

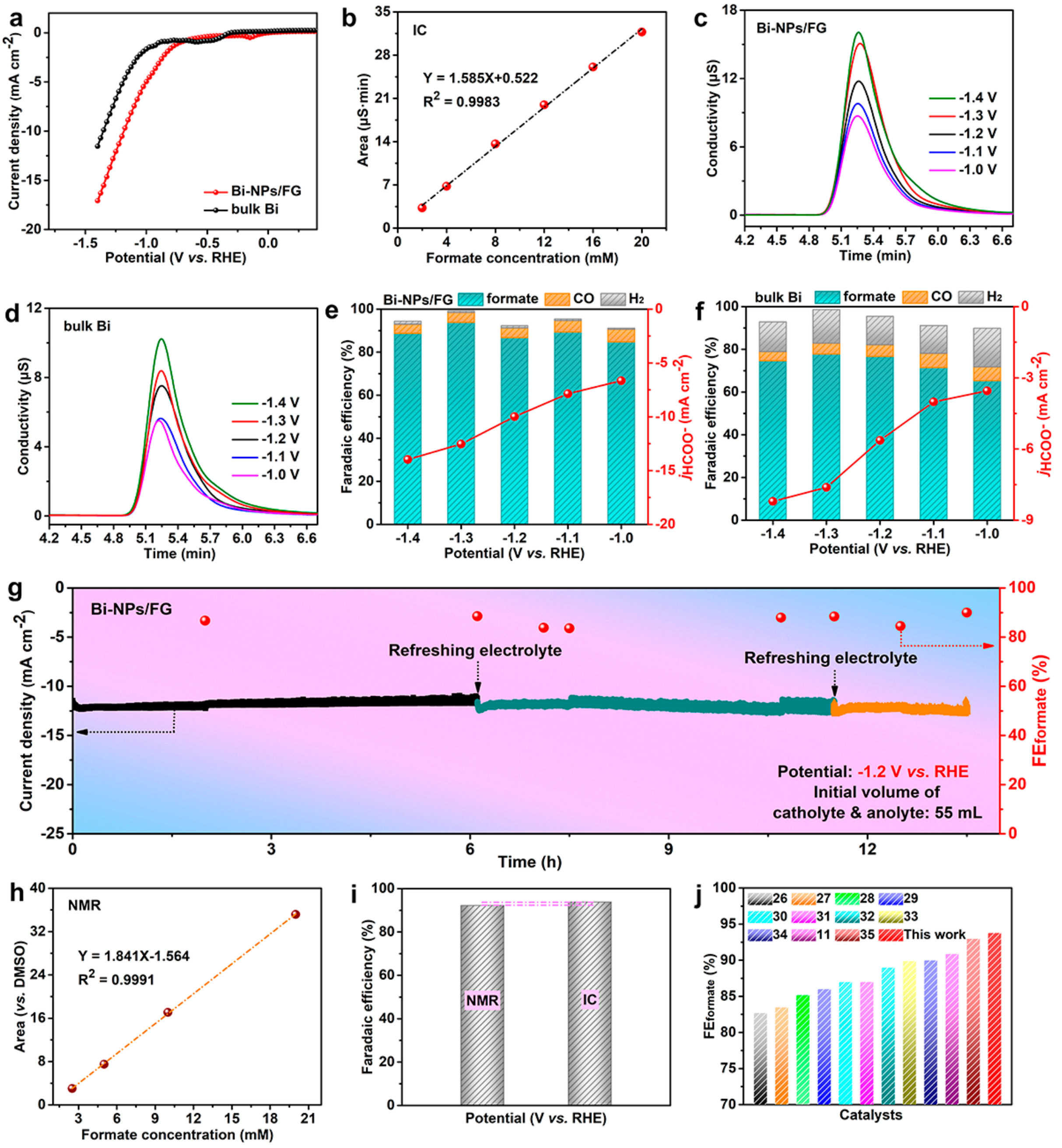

Figure 3. Electrocatalytic CO_2RR measurements in H-cell system. (a) LSV curves of Bi-NPs/FG composite and bulk Bi tested in CO_2-saturated 0.1 M $KHCO_3$ aqueous solution, respectively. (b) The standard curve with a concentration gradient for the quantitative analysis of formate content. (c, d) Ion chromatograms of the CO_2-saturated 0.1 M $KHCO_3$ electrolyte after the CO_2RR test of (c) Bi-NPs/FG composite and (d) bulk Bi at different applied potentials for 1 h, respectively. (e, f) Comparison of Faradaic efficiencies (left *Y* axes) and partial current densities (right *Y* axes) of the formate products between (e) Bi-NPs/FG composite and (f) bulk Bi, respectively. (g) Current density and $FE_{Formate}$ of Bi-NPs/FG composite during long-term CO_2 electroreduction reaction of 13.5 h at an applied potential of −1.2 V (vs. RHE). (h) Linear relationship between the different concentrations of formate and relative area (vs. DMSO). (i) Comparison of Faradaic efficiencies for formate at −1.3 V (vs. RHE) using Bi-NPs@FG catalyst between ^1H NMR and IC results. (j) Comparisons of $FE_{Formate}$ for Bi-NPs@FG with other catalysts reported in the previous literatures.

in Figure 2b. While traditional exfoliated graphene typically yields thin and flat nanosheets, the TEM image of FG in Figure 2c demonstrates cluster structures in the form of crumpled nanoflakes with a smooth surface, exhibiting a uniform size with dimensions of tens of nanometers. The use of FJH method significantly accelerates the transformation of CB to a high-quality FG phase, and this manifests in the resulting morphology of multilayered twisted/wrinkled FG with a thickness of 9−12 layers. The interlayer spacing, determined by the corresponding HRTEM image of the FG moiety in Figure 2c, is approximately 3.51 Å.

The electrocatalytic activities of both Bi-NPs/FG composite and bulk Bi toward the CO_2RR were evaluated in a high purity CO_2-saturated 0.1 M $KHCO_3$ aqueous solution using a typical H-type cell. The schematic of the experimental setup is illustrated in Figure S2. The two compartments were separated

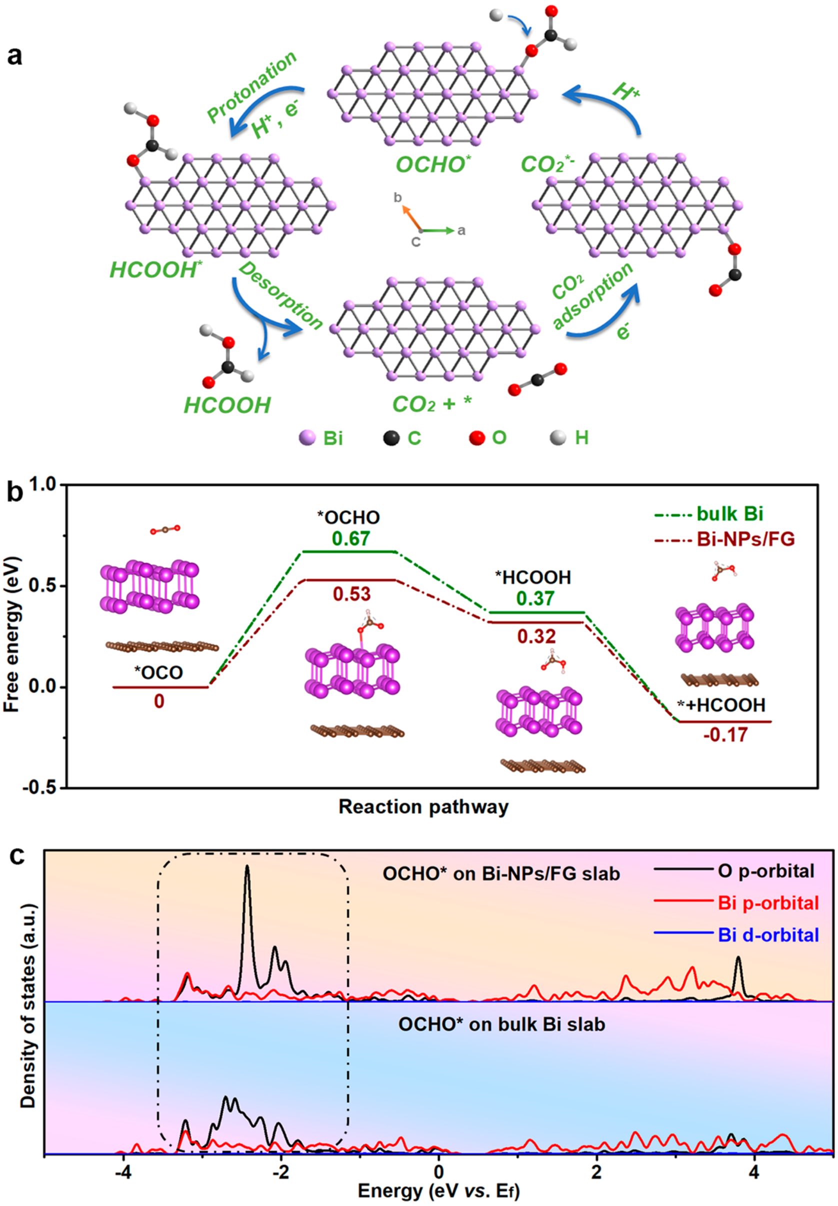

Figure 4. (a) Proposed reaction pathways of the electrocatalytic CO_2 reduction pathway on Bi crystal. (b) The calculated free-energy diagram of electrocatalytic CO_2 reduction pathway. The insets illustrate the adsorption configurations of the key intermediates. (c) PDOS of the OCHO* intermediates adsorbed on the Bi-NPs/FG and bulk Bi slabs.

by a Nafion-117 proton exchange membrane, and the working electrode was preactivated by cyclic voltammetry (CV) scans for 20 cycles at a scan rate of 50 mV/s in the potential range from 0 to −2.0 V (vs. Ag/AgCl) before the electrochemical test. Prior to the test, a high purity Ar_2 flow was continuously bubbled into the electrolyte. We present the linear sweep voltammetry (LSV) curve of the samples measured in a CO_2-saturated electrolyte in Figure 3a, which indicates that the Bi-NPs/FG composite exhibits much higher current density and a reduced onset potential in comparison with the bulk Bi in the same applied potential range. To examine the catalytic activity of Bi-NPs/FG composite, we carried out the CO_2RR test at various potentials ranging from −1.0 to −1.4 V (vs. reversible hydrogen electrode, RHE), and the time-resolved current density of samples during an operation period of 1 h are shown in Figure S5. As expected, the current density enhanced monotonously when the applied potential became more negative. By analysis of the final product using gas chromatography (GC) and ion chromatography (IC), the product compositions were found to be predominately formate and a trace amount of CO and H_2 over the whole potential range. The calibration curve is provided in Figure 3b, showing a good linear relationship between the peak area and the concentrations of formate. The accurate formate concentration of the final product was quantitatively detected by IC (Figure 3(c−d)). The Faradaic efficiencies of different products, accompanied by the corresponding partial current densities for formate, were plotted against applied potentials, as shown in Figure 3e. The Bi-NPs/FG composite possesses an extraordinarily high $FE_{Formate}$ at different applied potentials, where values of ~90% $FE_{Formate}$ over a broad potential were achieved. Notably, it reached a maximum $FE_{Formate}$ of 93.8% at −1.3 V (vs. RHE) and delivered a high current density of 12.6 mA cm^{-2}. In addition, the CO_2RR tests of the control sample

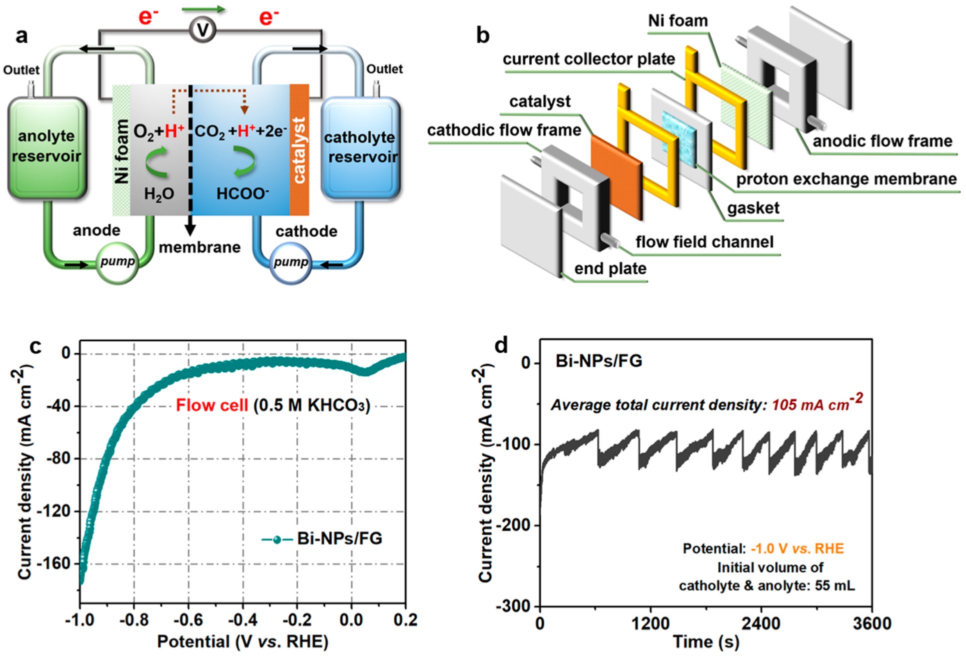

Figure 5. Flow cell tests. (a, b) Schematic diagram of a flow cell system for the electrocatalytic CO_2RR. (c) Linear sweep voltammetry (scan rate: 5 mV s^{-1}) curve of the Bi-NPs/FG catalyst tested in CO_2-saturated 0.5 M $KHCO_3$ solution using the flow cell system. (d) The chronoamperometric response (*I*−*T* curve) of the Bi-NPs/FG catalyst for the CO_2RR in flow cell at −1.0 V (vs. RHE) as indicated.

(i.e., bulk Bi) under the same reaction conditions showed inferior performance on both $FE_{Formate}$ and selectivity (Figure 3f). It is proposed that the homogeneous dispersion of Bi-NPs with abundant active sites on FG plays a crucial role in hydrogenating CO_2 to a high-value-added chemical (i.e., formate). The bubbles released from the surface of the Bi-NPs/FG-modified electrode in the cathode compartment were strongly inhibited during the electrocatalytic process, suggesting that electrons were predominantly used in the selective generation of liquid products rather than competitive gaseous products (e.g., H_2 and CO), thus leading to a superior catalytic performance.

Durability is a key parameter in evaluating the robustness of electrocatalysts during long-term electrochemical reactions. During the electrolytic reaction of 13.5 h at −1.2 V (vs. RHE), CO_2 gas was purged into electrolyte (0.1 M $KHCO_3$) continuously to alleviate the fluctuation of the CO_2 stability test, accompanied by a stable production of formate with superior faradaic efficiency, as illustrated in Figure 3g. Additionally, the total current density represents no obvious attenuation, showing a good stability of the Bi-NPs/FG electrocatalyst during the long-term CO_2RR. The comparison of Faradaic efficiencies toward the formate production on Bi-NPs@FG catalyst between ^{1}H NMR and IC results is shown in Figure 3i, indicating no obvious data gap. The comparison of the Bi-NPs/FG-enabled CO_2RR performance with other reports demonstrates that our results outperform the most formate-producing catalysts in terms of parameters for Faradaic efficiency of formate, as shown in Figure 3j.[11,26−35]

We employed the Nyquist plots measured by electrochemical impedance spectroscopy (EIS) to gain further insight into the intrinsic electrochemical mechanism of this study. Specifically, we used them to characterize the electroconductivity of Bi-NPs/FG composite and bulk Bi, as shown in Figure S6a. The interfacial electron transfer resistance (R_{ct}) value of the Bi-NPs/FG composite (9.2 Ω) was found to be much smaller than that of bulk Bi (33.1 Ω). This difference indicates that the Bi-NPs/FG composite possesses a superior electron-transport capacity due to the introduction of FG, thus facilitating the formation of reaction intermediates in the CO_2RR. The equivalent circuit model, which comprises R_s (internal resistance between the electrode and electrolyte), CPE (constant phase element), and R_{ct} (charge transfer resistance), is displayed as an inset of Figure S6a.

The enhanced catalytic performances of the catalysts were further investigated via electrochemical surface area (ECSA) analysis. The rate-determining step, reaction kinetics, and competitive reaction pathways thus were identified. The CV curves of the samples were tested from −0.2 to −0.3 V vs. Ag/AgCl, as shown in Figure S6(b−c). The differences between the cathode and anode current densities at −0.25 V were plotted versus the corresponding scan rates to calculate the double-layer capacitance (C_{dl}). The C_{dl} value of the Bi-NPs/FG composite (0.31 mF cm^{-2}) was found to be nearly 7.7-fold greater than that of the bulk Bi (0.04 mF cm^{-2}). These results indicate that the Bi-NPs/FG catalyst is capable of offering more electrocatalytic active sites, ultimately leading to an improved CO_2RR activity (as demonstrated in Figure S6d).[36]

The above experimental results and mechanism study suggest that the Bi-NPs/FG composite exhibits a high level of activity and selectivity toward the CO_2RR, which could be attributed to the uniform dispersion of Bi-NPs on FG that synergistically facilitates electron transfer and increases the effective ECSA, thereby leading to a reduction in the formation energy of *OCHO and binding energy of *HCOOH, preferentially favoring the CO_2-to-formate conversion pathway.[37] Furthermore, the exposed high-index (012) planes (Figure 1c) of Bi-NPs serve as optimized catalytic active sites, enabling the lowering of activation barriers for elementary steps of the CO_2-to-formate conversion pathway, specifically $* + CO_2 + [H^+ + e^-] \rightarrow *OCHO$ and $*OCHO + [H^+ + e^-] \rightarrow *HCOOH$, contributing to enhanced selectivity toward formate production over other CO_2RR products.[38] Additionally, the protective FG matrix can inhibit the oxidation of encased metallic Bi-NPs and prevent electrocatalyst deactivation.

The possible CO_2 electroreduction pathways over the Bi crystal were proposed in Figure 4a. To obtain the intrinsic mechanism of the highly selective formate production on the Bi-NPs/FG catalyst, the reaction path of CO_2RR was studied by the density functional theory (DFT) calculations (Figure 4b) and the adsorption configurations of the key intermediates involved are depicted as insets in Figure 4b. In the two-electron process of the HCOOH production pathway, the rate-determining step (RDS) is identified as the proton coupled electron transfer of OCHO*.[29] Herein, the G_{OCHO*} value (0.53 eV) of Bi-NPs/FG is slightly lower than that (0.67 eV) of bulk Bi. For the Bi-NPs/FG model (Figure 4c), the dotted box area in the partial density of state (PDOS) indicates that there is a stronger contribution between the *p* orbital of the Bi atom and the *p* orbital of the O atom in the intermediate (OCHO*).[39] The adsorption affinity of OCHO* on the Bi-NPs/FG surface is stronger, thereby reducing the over potential of the reaction pathway. It can be concluded that the reconstruction process enhances the bonding strength of the surface Bi-OCHO* as well as optimizes the adsorption energy of the key intermediate (OCHO*), leading to a promotion of formate production.

To assess the commercial viability of the designed Bi-NPs/FG catalyst, we conducted the CO_2RR tests using a custom-made flow cell system, as depicted in Figure 5(a, b). The catalyst's performance was evaluated in 0.5 M $KHCO_3$ electrolyte saturated with high-purity CO_2 gas.[40] The linear sweep voltammetry (LSV) curve of the Bi-NPs/FG electrode displayed significantly higher current density compared to that of the H cell under the same potential range (Figure 5c). We examined the current density of the Bi-NPs/FG catalyst as a function of reaction time (1 h operational period), as shown in Figure 5d. The average total current density was found to be 105 mA cm^{-2}, with a Faradaic efficiency of approximately 57.3% toward formate at −1.0 V (vs. RHE), which may be attributed to the ultralow catalyst loading amount that cannot completely suppress the competing hydrogen evolution reaction (HER).

Furthermore, we carried out an extension study of the FJH route to demonstrate its versatility in diverse application scenarios. Through the addition of various metal salt precursors, we were able to prepare a range of metal/alloy NPs encased in FG, namely, unary metals (Cu and Pt) and high-entropy alloys (MnFeCoNiCuZn and PtPdRhRuAu). The XRD patterns of all synthesized samples in Figure S7(a−d) exhibited well-indexed Bragg peaks corresponding to a typical cubic structure with a space group of $Fm\bar{3}m$.[41,42] Notably, the (111), (200), and (220) planes of the face-centered cubic (fcc) structure were represented by three characteristic diffraction peaks. Furthermore, a peak shift to a lower degree was observed for nonprecious metal/alloy NPs (Cu-NPs/FG, MnFeCoNiCuZn-NPs/FG) compared to precious metal/alloy NPs (Pt-NPs/FG, PtPdRhRuAu-NPs/FG) due to the difference in atomic radius. Additionally, a significant decrease in the intensity of the characteristic peak (111) in XRD patterns for high-entropy alloy NPs was consistent with previous report.[41] Detailed HRTEM characterizations and EDX elemental mappings confirmed that both unary metal NPs (Cu, Pt) and high-entropy alloy NPs (MnFeCoNiCuZn, PtPdRhRuAu) exhibited uniform sizes, less than 50 nm in diameter regardless of the elemental compositions, and even distribution across the FG matrix (Figure S7(a-d) and Figure S8). The element ratios of as-synthesized FG supported metal/alloy NPs samples were derived from X-ray photoelectron spectroscopy (XPS) analysis, as displayed in Table S3. In addition, we carried out tests for electrocatalytic performance on water splitting of metal/alloy NPs wrapped by FG, and the corresponding results along with a brief introduction are shown in Figure S9.

In summary, this study introduces a highly efficient and rapid FJH route for producing metal NPs enveloped by FG for the first time. The in situ formation of Bi-NPs encased in FG needs less than 200 ms to complete the reaction. The designed Bi-NPs/FG composite exhibits a high selectivity and superior electrocatalytic CO_2-to-formate Faradaic efficiency of 93.8% at −1.3 V vs. RHE, and show good long-term durability due to the synergistic effect. DFT calculations suggest that the maintenance of the high activity for formate production over the Bi-NPs/FG catalyst is mainly attributed to the reconstructive process that enhances the bond energy of the surface Bi-OCHO* and optimizes the absorption capacity of the crucial OCHO* intermediate. In a further extension study, the FJH method was successfully extended to other systems, achieving the preparation of a series of precious and nonprecious metal/alloy NPs (such as Cu, Pt, MnFeCoNiCuZn, and PtPdRhRuAu) wrapped in FG. These findings provide a promising ultrafast and environment-friendly avenue for constructing novel metal-based electrode materials with FG support in domains of batteries, ammonium synthesis, water splitting, and biomass valorization.

■ ASSOCIATED CONTENT

Supporting Information

The Supporting Information is available free of charge at https://pubs.acs.org/doi/10.1021/acsmaterialslett.3c01183.

> Experimental section; computational details; digital photograph of the FJH equipment; XPS spectra; particle size distribution data; *I*−*T* curves; EIS analysis; CV curves; structure information for extended FG supported metal/alloy NPs; elemental ratios of samples; electrocatalytic water splitting performances; Figures S1−S9; Tables S1−S3; and supporting references (PDF)

■ AUTHOR INFORMATION

Corresponding Authors

Jing Ma − *State Key Laboratory of Coordination Chemistry, MOE Key Laboratory of Mesoscopic Chemistry, MOE Key Laboratory of High Performance Polymer Materials and Technology, Jiangsu Key Laboratory of Advanced Organic Materials, School of Chemistry and Chemical Engineering, Nanjing University, Nanjing, Jiangsu 210023, China;* orcid.org/0000-0001-5848-9775; Email: majing@nju.edu.cn

Zhong Jin − *State Key Laboratory of Coordination Chemistry, MOE Key Laboratory of Mesoscopic Chemistry, MOE Key Laboratory of High Performance Polymer Materials and Technology, Jiangsu Key Laboratory of Advanced Organic Materials, School of Chemistry and Chemical Engineering, Nanjing University, Nanjing, Jiangsu 210023, China;* orcid.org/0000-0001-8860-8579; Email: zhongjin@nju.edu.cn

Authors

Miao Wang − *State Key Laboratory of Coordination Chemistry, MOE Key Laboratory of Mesoscopic Chemistry, MOE Key Laboratory of High Performance Polymer Materials and Technology, Jiangsu Key Laboratory of Advanced Organic Materials, School of Chemistry and Chemical Engineering, Nanjing University, Nanjing, Jiangsu 210023, China*

Huaizhu Wang − *State Key Laboratory of Coordination Chemistry, MOE Key Laboratory of Mesoscopic Chemistry, MOE Key Laboratory of High Performance Polymer Materials and Technology, Jiangsu Key Laboratory of Advanced Organic Materials, School of Chemistry and Chemical Engineering, Nanjing University, Nanjing, Jiangsu 210023, China*

Yating Gu − *State Key Laboratory of Coordination Chemistry, MOE Key Laboratory of Mesoscopic Chemistry, MOE Key Laboratory of High Performance Polymer Materials and Technology, Jiangsu Key Laboratory of Advanced Organic Materials, School of Chemistry and Chemical Engineering, Nanjing University, Nanjing, Jiangsu 210023, China*

Mengfei Zhu − *State Key Laboratory of Coordination Chemistry, MOE Key Laboratory of Mesoscopic Chemistry, MOE Key Laboratory of High Performance Polymer Materials and Technology, Jiangsu Key Laboratory of Advanced Organic Materials, School of Chemistry and Chemical Engineering, Nanjing University, Nanjing, Jiangsu 210023, China*

Mohan Kumar − *Department of Chemistry, PES Institute of Technology and Management, Kotegangoor 577204 Shivamogga, India;* orcid.org/0000-0003-1986-6384

Junchuan Liang − *State Key Laboratory of Coordination Chemistry, MOE Key Laboratory of Mesoscopic Chemistry, MOE Key Laboratory of High Performance Polymer Materials and Technology, Jiangsu Key Laboratory of Advanced Organic Materials, School of Chemistry and Chemical Engineering, Nanjing University, Nanjing, Jiangsu 210023, China; Nanjing Tieming Energy Technology Co., Ltd., Nanjing, Jiangsu 210093, P. R. China; Suzhou Tierui New Energy Technology Co., Ltd., Suzhou, Jiangsu 215228, P. R. China; Jiangsu BTR Nano Technology Co., Ltd., Changzhou, Jiangsu 213200, P. R. China*

Zuoxiu Tie − *State Key Laboratory of Coordination Chemistry, MOE Key Laboratory of Mesoscopic Chemistry, MOE Key Laboratory of High Performance Polymer Materials and Technology, Jiangsu Key Laboratory of Advanced Organic Materials, School of Chemistry and Chemical Engineering, Nanjing University, Nanjing, Jiangsu 210023, China*

Complete contact information is available at:
https://pubs.acs.org/10.1021/acsmaterialslett.3c01183

Author Contributions

[#]These authors contributed equally to this work. CRediT: **Miao Wang** conceptualization, data curation, formal analysis, investigation, methodology, writing-original draft, writing-review & editing; **Huaizhu Wang** data curation, formal analysis, methodology; **Yating Gu** formal analysis, methodology, software, writing-original draft; **Mengfei Zhu** data curation; **Mohan Kumar** writing-original draft; **Junchuan Liang** data curation; **Zuoxiu Tie** supervision, writing-review & editing; **Jing Ma** formal analysis, investigation, methodology, resources, writing-review & editing; **Zhong Jin** conceptualization, funding acquisition, investigation, methodology, project administration, resources, supervision, validation, visualization, writing-review & editing.

Notes

The authors declare no competing financial interest.

■ ACKNOWLEDGMENTS

The authors appreciate the financial support from the National Natural Science Foundation of China (Nos. 22022505 and 22033004), the Fundamental Research Funds for the Central Universities of China (Nos. 020514380266, 020514380272 and 020514380274), the Scientific and Technological Innovation Special Fund for Carbon Peak and Carbon Neutrality of Jiangsu Province (No. BK20220008), the Scientific and Technological Achievements Transformation Special Fund of Jiangsu Province (No. BA2023037), the International Collaboration Research Program of Nanjing City (Nos. 202201007 and 2022SX00000955), and the Gusu Leading Talent Program of Scientific and Technological Innovation and Entrepreneurship of Wujiang District in Suzhou City (No. ZXL2021273). We also thank the High Performance Computing Centre of Nanjing University for providing the IBM Blade cluster system.

■ REFERENCES

(1) Cox, P. M.; Betts, R. A.; Jones, C. D.; Spall, S. A.; Totterdell, I. J. Acceleration of Global Warming Due to Carbon-Cycle Feedbacks in a Coupled Climate Model. *Nature* **2000**, *408*, 184−187.

(2) Sultan, S.; Tiwari, J. N.; Singh, A. N.; Zhumagali, S.; Ha, M.; Myung, C. W.; Thangavel, P.; Kim, K. S. Single Atoms and Clusters Based Nanomaterials for Hydrogen Evolution, Oxygen Evolution Reactions, and Full Water Splitting. *Adv. Energy Mater.* **2019**, *9*, 1900624−1900672.

(3) Ledendecker, M.; Clavel, G.; Antonietti, M.; Shalom, M. Highly Porous Materials as Tunable Electrocatalysts for the Hydrogen and Oxygen Evolution Reaction. *Adv. Funct. Mater.* **2015**, *25*, 393−399.

(4) Wong, S. S.; Shu, R.; Zhang, J.; Liu, H.; Yan, N. Downstream Processing of Lignin Derived Feedstock into End Products. *Chem. Soc. Rev.* **2020**, *49*, 5510−5560.

(5) Wijaya, Y. P.; Smith, K. J.; Kim, C. S.; Gyenge, E. L. Synergistic Effects between Electrocatalyst and Electrolyte in the Electrocatalytic Reduction of Lignin Model Compounds in a Stirred Slurry Reactor. *J. Appl. Electrochem.* **2021**, *51*, 51−63.

(6) Birdja, Y. Y.; Pérez-Gallent, E.; Figueiredo, M. C.; Göttle, A. J.; Calle-Vallejo, F.; Koper, M. T. M. Advances and Challenges in Understanding the Electrocatalytic Conversion of Carbon Dioxide to Fuels. *Nature Energy* **2019**, *4*, 732−745.

(7) Zhang, W.; Hu, Y.; Ma, L.; Zhu, G.; Wang, Y.; Xue, X.; Chen, R.; Yang, S.; Jin, Z. Progress and Perspective of Electrocatalytic CO_2 Reduction for Renewable Carbonaceous Fuels and Chemicals. *Advanced Science* **2018**, *5*, 1700275−1700299.

(8) Grubel, K.; Jeong, H.; Yoon, C. W.; Autrey, T. Challenges and Opportunities for Using Formate to Store, Transport, and Use Hydrogen. *J. Energy Chem.* **2020**, *41*, 216−224.

(9) An, L.; Chen, R. Direct Formate Fuel Cells: A Review. *J. Power Sources* **2016**, *320*, 127−139.

(10) Greeley, J.; Jaramillo, T. F.; Bonde, J.; Chorkendorff, I.; Nørskov, J. K. Computational High-Throughput Screening of Electrocatalytic Materials for Hydrogen Evolution. *Nat. Mater.* **2006**, *5*, 909−913.

(11) Zhang, W.; Yang, S.; Jiang, M.; Hu, Y.; Hu, C.; Zhang, X.; Jin, Z. Nanocapillarity and Nanoconfinement Effects of Pipet-like Bismuth@Carbon Nanotubes for Highly Efficient Electrocatalytic CO_2 Reduction. *Nano Lett.* **2021**, *21*, 2650−2657.

(12) Wu, M.; Xu, B.; Zhang, Y.; Qi, S.; Ni, W.; Hu, J.; Ma, J. Perspectives in Emerging Bismuth Electrochemistry. *Chem. Eng. J.* **2020**, *381*, 122558−122575.

(13) Luong, D. X.; Bets, K. V.; Algozeeb, W. A.; Stanford, M. G.; Kittrell, C.; Chen, W.; Salvatierra, R. V.; Ren, M.; McHugh, E. A.; Advincula, P. A.; Wang, Z.; Bhatt, M.; Guo, H.; Mancevski, V.; Shahsavari, R.; Yakobson, B. I.; Tour, J. M. Gram-Scale Bottom-up Flash Graphene Synthesis. *Nature* **2020**, *577*, 647−651.

(14) Algozeeb, W. A.; Savas, P. E.; Luong, D. X.; Chen, W.; Kittrell, C.; Bhat, M.; Shahsavari, R.; Tour, J. M. Flash Graphene from Plastic Waste. *ACS Nano* **2020**, *14*, 15595−15604.

(15) Deng, B.; Luong, D. X.; Wang, Z.; Kittrell, C.; McHugh, E. A.; Tour, J. M. Urban Mining by Flash Joule Heating. *Nat. Commun.* **2021**, *12*, 5794−5802.

(16) Deng, B.; Wang, X.; Luong, D. X.; Carter, R. A.; Wang, Z.; Tomson, M. B.; Tour, J. M. Rare Earth Elements from Waste. *Science Advances* **2022**, *8*, 3132−3141.

(17) Chen, W.; Ge, C.; Li, J. T.; Beckham, J. L.; Yuan, Z.; Wyss, K. M.; Advincula, P. A.; Eddy, L.; Kittrell, C.; Chen, J.; Luong, D. X.; Carter, R. A.; Tour, J. M. Heteroatom-Doped Flash Graphene. *ACS Nano* **2022**, *16*, 6646−6656.

(18) Zhu, S.; Zhang, F.; Lu, H.-G.; Sheng, J.; Wang, L.; Li, S.-D.; Han, G.; Li, Y. Flash Nitrogen-Doped Graphene for High-Rate Supercapacitors. *ACS Materials Lett.* **2022**, *4*, 1863−1871.

(19) Wyss, K. M.; Li, J. T.; Advincula, P. A.; Bets, K. V.; Chen, W.; Eddy, L.; Silva, K. J.; Beckham, J. L.; Chen, J.; Meng, W.; Deng, B.; Nagarajaiah, S.; Yakobson, B. I.; Tour, J. M. Upcycling of Waste Plastic into Hybrid Carbon Nanomaterials. *Adv. Mater.* **2023**, *35*, 2209621−2209635.

(20) Stanford, M. G.; Bets, K. V.; Luong, D. X.; Advincula, P. A.; Chen, W.; Li, J. T.; Wang, Z.; McHugh, E. A.; Algozeeb, W. A.; Yakobson, B. I.; Tour, J. M. Flash Graphene Morphologies. *ACS Nano* **2020**, *14*, 13691−13699.

(21) Barbhuiya, N. H.; Kumar, A.; Singh, A.; Chandel, M. K.; Arnusch, C. J.; Tour, J. M.; Singh, S. P. The Future of Flash Graphene for the Sustainable Management of Solid Waste. *ACS Nano* **2021**, *15*, 15461−15470.

(22) Malard, L. M.; Pimenta, M. A.; Dresselhaus, G.; Dresselhaus, M. S. Raman Spectroscopy in Graphene. *Phys. Rep.* **2009**, *473*, 51−87.

(23) Zhang, E.; Wang, T.; Yu, K.; Liu, J.; Chen, W.; Li, A.; Rong, H.; Lin, R.; Ji, S.; Zheng, X.; Wang, Y.; Zheng, L.; Chen, C.; Wang, D.; Zhang, J.; Li, Y. Bismuth Single Atoms Resulting from Transformation of Metal-Organic Frameworks and Their Use as Electrocatalysts for CO_2 Reduction. *J. Am. Chem. Soc.* **2019**, *141*, 16569−16573.

(24) Gao, J.; Wang, Y.; Wu, H.; Liu, X.; Wang, L.; Yu, Q.; Li, A.; Wang, H.; Song, C.; Gao, Z.; Peng, M.; Zhang, M.; Ma, N.; Wang, J.; Zhou, W.; Wang, G.; Yin, Z.; Ma, D. Construction of a sp^3/sp^2 Carbon Interface in 3D N-Doped Nanocarbons for the Oxygen Reduction Reaction. *Angew. Chem., Int. Ed.* **2019**, *58*, 15089−15097.

(25) Díaz, J.; Paolicelli, G.; Ferrer, S.; Comin, F. Separation of the sp^3 and sp^2 Components in the C_{1s} Photoemission Spectra of Amorphous Carbon Films. *Phys. Rev. B* **1996**, *54*, 8064−8069.

(26) Chen, Z.; Yao, S.; Liu, L. 3D Hierarchical Porous Structured Carbon Nanotube Aerogel-Supported Sn Spheroidal Particles: An Efficient and Selective Catalyst for Electrochemical Reduction of CO_2 to Formate. *Journal of Materials Chemistry A* **2017**, *5*, 24651−24656.

(27) Han, N.; Wang, Y.; Deng, J.; Zhou, J.; Wu, Y.; Yang, H.; Ding, P.; Li, Y. Self-Templated Synthesis of Hierarchical Mesoporous SnO_2 Nanosheets for Selective CO_2 Reduction. *Journal of Materials Chemistry A* **2019**, *7*, 1267−1272.

(28) Yi, L.; Chen, J.; Shao, P.; Huang, J.; Peng, X.; Li, J.; Wang, G.; Zhang, C.; Wen, Z. Molten-Salt-Assisted Synthesis of Bismuth Nanosheets for Long-Term Continuous Electrocatalytic Conversion of CO_2 to Formate. *Angew. Chem., Int. Ed.* **2020**, *59*, 20112−20119.

(29) Zhang, W.; Hu, Y.; Ma, L.; Zhu, G.; Zhao, P.; Xue, X.; Chen, R.; Yang, S.; Ma, J.; Liu, J.; et al. Liquid-Phase Exfoliated Ultrathin Bi Nanosheets: Uncovering the Origins of Enhanced Electrocatalytic CO_2 Reduction on Two-Dimensional Metal Nanostructure. *Nano energy* **2018**, *53*, 808−816.

(30) Tran-Phu, T.; Daiyan, R.; Fusco, Z.; Ma, Z.; Amal, R.; Tricoli, A. Nanostructured β-Bi_2O_3 Fractals on Carbon Fibers for Highly Selective CO_2 Electroreduction to Formate. *Adv. Funct. Mater.* **2020**, *30*, 1906478−1906486.

(31) Li, F.; Chen, L.; Knowles, G. P.; MacFarlane, D. R.; Zhang, J. Hierarchical Mesoporous SnO_2 Nanosheets on Carbon Cloth: A Robust and Flexible Electrocatalyst for CO_2 Reduction with High Efficiency and Selectivity. *Angew. Chem., Int. Ed.* **2017**, *56*, 505−509.

(32) Lei, F.; Liu, W.; Sun, Y.; Xu, J.; Liu, K.; Liang, L.; Yao, T.; Pan, B.; Wei, S.; Xie, Y. Metallic Tin Quantum Sheets Confined in Graphene toward High-Efficiency Carbon Dioxide Electroreduction. *Nat. Commun.* **2016**, *7*, 12697−12705.

(33) Peng, L.; Wang, Y.; Wang, Y.; Xu, N.; Lou, W.; Liu, P.; Cai, D.; Huang, H.; Qiao, J. Separated Growth of Bi-Cu Bimetallic Electrocatalysts on Defective Copper Foam for Highly Converting CO_2 to Formate with Alkaline Anion-Exchange Membrane beyond $KHCO_3$ Electrolyte. *Appl. Catal. B: Environmental* **2021**, *288*, 120003−120012.

(34) Ren, B.; Wen, G.; Gao, R.; Luo, D.; Zhang, Z.; Qiu, W.; Ma, Q.; Wang, X.; Cui, Y.; Ricardez-Sandoval, L.; et al. Nano-Crumples Induced Sn-Bi Bimetallic Interface Pattern with Moderate Electron Bank for Highly Efficient CO_2 Electroreduction. *Nat. Commun.* **2022**, *13*, 2486−2497.

(35) Zheng, X.; De Luna, P.; García de Arquer, F. P.; Zhang, B.; Becknell, N.; Ross, M. B.; Li, Y.; Banis, M. N.; Li, Y.; Liu, M.; et al. Sulfur-Modulated Tin Sites Enable Highly Selective Electrochemical Reduction of CO_2 to Formate. *Joule* **2017**, *1*, 794−805.

(36) Gao, S.; Lin, Y.; Jiao, X.; Sun, Y.; Luo, Q.; Zhang, W.; Li, D.; Yang, J.; Xie, Y. Partially Oxidized Atomic Cobalt Layers for Carbon Dioxide Electroreduction to Liquid Fuel. *Nature* **2016**, *529*, 68−71.

(37) Gong, Q.; Ding, P.; Xu, M.; Zhu, X.; Wang, M.; Deng, J.; Ma, Q.; Han, N.; Zhu, Y.; Lu, J.; Feng, Z.; Li, Y.; Zhou, W.; Li, Y. Structural Defects on Converted Bismuth Oxide Nanotubes Enable Highly Active Electrocatalysis of Carbon Dioxide Reduction. *Nat. Commun.* **2019**, *10*, 2807−2817.

(38) Koh, J. H.; Won, D. H.; Eom, T.; Kim, N.-K.; Jung, K. D.; Kim, H.; Hwang, Y. J.; Min, B. K. Facile CO_2 Electro-Reduction to Formate via Oxygen Bidentate Intermediate Stabilized by High-Index Planes of Bi Dendrite Catalyst. *ACS Catal.* **2017**, *7*, 5071−5077.

(39) Zhang, A.; Liang, Y.; Li, H.; Zhao, X.; Chen, Y.; Zhang, B.; Zhu, W.; Zeng, J. Harmonizing the Electronic Structures of the Adsorbate and Catalysts for Efficient CO_2 Reduction. *Nano Lett.* **2019**, *19*, 6547−6553.

(40) Wei, X.; Li, Z.; Jang, H.; Kim, M.-G.; Qin, Q.; Liu, X. Lattice Strain and Interfacial Engineering of a Bi-based Electrocatalyst for Highly Selective CO_2 Electroreduction to Formate. *Science China Materials* **2023**, *66*, 1398−1406.

(41) Yao, Y.; Huang, Z.; Xie, P.; Lacey, S. D.; Jacob, R. J.; Xie, H.; Chen, F.; Nie, A.; Pu, T.; Rehwoldt, M.; Yu, D.; Zachariah, M. R.; Wang, C.; Shahbazian-Yassar, R.; Li, J.; Hu, L. Carbothermal Shock Synthesis of High-Entropy-Alloy Nanoparticles. *Science* **2018**, *359*, 1489−1494.

(42) Li, T.; Dong, Q.; Huang, Z.; Wu, L.; Yao, Y.; Gao, J.; Wang, X.; Zhang, H.; Wang, D.; Li, T.; Shahbazian-Yassar, R.; Hu, L. Interface Engineering Between Multi-Elemental Alloy Nanoparticles and a Carbon Support Toward Stable Catalysts. *Adv. Mater.* **2022**, *34*, 2106436−2106441.

https://doi.org/10.1021/acsmaterialslett.3c01183
ACS Materials Lett. 2024, 6, 100−108